



Surface grain boundary engineering in 304 stainless steel by means of mechanical grinding treatment-induced gradient plastic strain and annealing

Xinli Jiang¹, Chongwen Yang¹, Wenqian Zhang², and Xuelin Wang^{1,*}

¹ State Key Lab of Digital Manufacturing Equipment and Technology, School of Mechanical Science and Engineering, Huazhong University of Science and Technology, Wuhan 430074, China

² Hubei Key Laboratory of Modern Manufacturing Quality Engineering, School of Mechanical Engineering, Hubei University of Technology, Wuhan 430074, China

Received: 26 September 2022

Accepted: 16 November 2022

Published online:

24 November 2022

© The Author(s), under exclusive licence to Springer Science+Business Media, LLC, part of Springer Nature 2022

ABSTRACT

Grain boundary engineering (GBE) has shown a promising application in improving resistance to intergranular corrosion (IGC) of polycrystalline metallic materials with low-stacking fault energy, such as austenitic stainless steels. However, the traditionally uniform plastic pre-straining methods, such as cold rolling, in thermomechanical processing are hard to implement on complicated surfaces. Here, we demonstrate a novel approach using gradient plastic strain induced by surface mechanical grinding treatment with a rotary tool and subsequent annealing to optimize grain boundary character distribution (GBCD) in the near-surface layer. The gradient plastic strain followed by long-time annealing (24–96 h) in 304 stainless steels achieved an optimized GBCD with over 75% frequency of coincidence site lattice (CSL) boundaries and disconnected random boundary network in the near-surface layer. The intergranular corrosion tests showed that the resulting 304 stainless steels with the optimized GBCD in the near-surface layer present an excellent resistance to IGC behavior due to a high fraction of $\Sigma 3^n$ boundaries. During the annealing process, severe plastic strain near the surface results in small size grain clusters via strain recrystallization, while low-level plastic strain in the subsurface promotes the formation of high fraction of CSL boundaries and large size grain clusters via strain-induced boundary migration. After the complete depletion of gradient plastic strain, the directional growth of grain clusters promotes the further extension of surface GBE into interior region. Thus, the thickness of surface GBE region can be regulated by the annealing time.

Handling Editor: Sophie Primig

Address correspondence to E-mail: wangxl@hust.edu.cn

Introduction

The optimization of grain boundary character distribution (GBCD) through grain boundary engineering (GBE) has been developed in the last two decades since Watanabe proposed the concept of grain boundary design and control [1–4]. As a kind of thermomechanical treatment, GBE has been shown a high potential to suppress the intergranular corrosion (IGC) [5, 6], intergranular stress corrosion cracking (IGSCC) [7, 8], hydrogen embrittlement [9] and fatigue fracture [10, 11]. The improvement of these related properties can be achieved by introducing high frequencies of low coincidence site lattice (CSL) boundaries and disrupting the connected random boundary network via proper thermomechanical treatments [12, 13]. The CSL boundaries, especially twin boundaries, have shown better performance on ductility [14], fracture [15] and corrosion resistance [16] than random boundaries.

Uniform plastic pre-straining methods, such as cold rolling and uniaxial tension/compression, have been vastly implemented in thermomechanical processing for bulk materials [17–20]. These thermomechanical treatments have evolved over recent years and can be roughly classified into strain recrystallization and strain annealing process based on the strain level [21]. For example, Lehockey et al. [22] used multi-step strain recrystallization process to improve the weldability in nickel-based and iron-based superalloys. Thaveerungsriporn et al. [23] showed the effect of iterative strain annealing on grain boundary network of 304 stainless steels. Kumar et al. [24] have reported that the fraction of special boundaries in Cu and Inconel 600 could be substantially increased by strain recrystallization process. Low-level pre-strain with annealing has also shown the potential to optimize the GBCD in austenitic stainless steels [25] and nickel-based alloys [7]. Yang et al. [26] achieved the optimization of GBCD during the low-strain GBE by strain-induced boundary migration in pure copper. Despite these applications, these traditionally uniform pre-straining methods in thermomechanical processing have become a bottleneck for the applications of GBE to components with complex surface shapes.

Surface GBE has been applied for improving the resistance to IGC and IGSCC by localized surface thermomechanical process on stainless steel surface.

For the improvement of surface IGC resistance, Yang et al. [27] applied laser surface melting with annealing treatment to optimize GBCD on the surface of 304 stainless steel. Alyousif et al. [28] attempted to apply shot peening followed by annealing for controlling the near-surface microstructure of 304 stainless steel. Tokita et al. [29] applied laser peening as a pre-straining method during thermomechanical treatments to introduce suitable pre-strain into surface of 304 stainless steel. Telang et al. [30] used iterative cycles of ultrasonic nanocrystal surface modification with strain annealing to optimize the near-surface microstructure in Alloy 600. Their results indicate that the surface Cr depletion and IGSCC were both suppressed by the increased fraction of special grain boundaries.

Surface mechanical machining, an indispensable fabrication process, has vast implementation in the industrial community to produce desired shapes and dimensions of components [31]. As a method of machining-induced surface plastic deformation, the surface mechanical grinding treatment (SMGT) has great potential to produce gradient nanostructures with gradient plastic strain in the surface layer [32, 33]. Compared to these local surface pre-straining methods, the SMGT treatment with a rotary tool exhibits a prominently gradient distribution of applied plastic strain and accumulated total plastic strain from the top surface to the interior by one pass processing. Uniformly distributed in-plane plastic deformation can be introduced into the surface layer at a high shear strain rate while retaining the flatness of surface. Here, we demonstrate a novel approach to optimize GBCD of the near-surface layer in 304 stainless steel using gradient plastic pre-strain induced by SMGT with a rotary tool and subsequent annealing. Furthermore, the effect of optimized GBCD in the near-surface layer on the IGC resistance and the evolution of microstructure under gradient plastic strain during annealing are presented and discussed.

Experimental methods

The material used in this study was a commercial 304 austenitic stainless steel with the chemical composition (wt.%) of 19.15 Cr, 8.2 Ni, 0.44 Si, 1.57 Mn, 0.0389 C and 0.0225 P. The as-received material was in solution-heat-treated condition and labeled as the

base material (BM). A rectangular specimen with dimensions of 80 mm × 40 mm × 10 mm was prepared using an electric discharge. The thermomechanical treatment was performed using SMGT as a surface gradient plastic pre-straining method and subsequent annealing. A schematic of the SMGT process following a surface milling at ambient temperature is illustrated in Fig. 1. During the SMGT process, a diamond tip with a high rotating speed (v_1) penetrates tens of micrometers into surface and then slides the axial direction of the sample at a relatively low speed (v_2). The SMGT-induced severe plastic strain in the surface layer and the depth of deformation layer are mainly determined by the penetration depth a_p , as shown in Fig. 1(b). The SMGT processing with one pass was carried out on a 80 mm × 40 mm surface area of BM specimens under coolant using a vertical CNC machining center. The processing parameters were set as follows: $v_1 = 300$ r/min, $v_2 = 300$ mm/min, $r = 6$ mm and $a_p = 20$ μm, 40 μm and 60 μm, respectively. The pre-strained specimens by SMGT were annealed at 900 °C for 24–96 h followed by water quenched and labeled as SMGT-induced grain boundary engineering material (SMGT-GBEM).

The frequency of CSL boundaries and the GBCD were analyzed by orientation imaging microscopy (OIM) with GeminiSEM300 field emission scanning

electron microscope with a step size of 1–3 μm. The grain boundaries with $\Sigma \leq 29$ were classified as CSL boundaries and the other boundaries were classified as random boundaries [34]. The $\Sigma 3^n$ ($n \geq 1$) grain boundaries were classified as special boundaries due to their excellent corrosion resistance. The CSL% values were calculated as a length ratio of grain boundaries with $\Sigma \leq 29$ to all the boundaries in the analyzed region. Brandon's criterion [35] was adopted for critical deviation in the grain boundary characterization [36]. The cross-sectional microhardness measurements were performed along the depth of SMGT specimens from surface using an automatic Vickers hardness tester. A test force of 200 gf was applied with a holding time of 10 s. To avoid the mutual influence among the tested points, the distance between any two measured points was at least five times the Vickers diagonal length. The intergranular corrosion susceptibilities of the BM and SMGT-GBEM specimens were assessed by performing ferric sulfate-sulfuric acid test and oxalic acid electrochemical corrosion test after sensitizing at 650 °C for 2 h. Ferric sulfate-sulfuric acid test was carried out in a boiling solution of 6.8 mol/L H_2SO_4 plus 0.1 mol/L $\text{Fe}_2(\text{SO}_4)_3$ for 72 h [37]. The specimens were etched in 10 wt.% oxalic acid solution under 1 A/cm² current density for 60 s in oxalic acid electrochemical corrosion test. The surface and cross section corrosion micrographs were observed by Olympus DSX 510 optical microscopy and scanning electron microscopy (SEM).

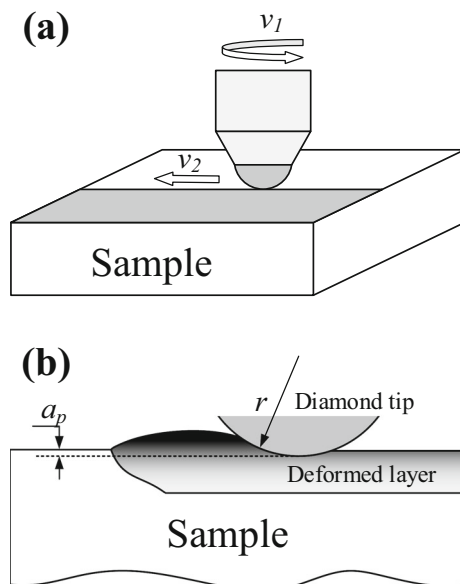


Figure 1 Schematic illustrations of **a** the SMGT processing with a rotary tool on the milled surface and **b** the SMGT-induced plastic deformation layer.

Results and discussion

Optimization of GBCD in the near-surface layer

The GBCD and inverse pole figure (IPF) maps of BM observed by using EBSD are presented in Fig. 2. The special boundaries for $\Sigma 3$, $\Sigma 9$, $\Sigma 27$ and other CSL boundaries are shown by red, blue, green and turquoise lines, respectively. The random boundaries (R) shown by black lines are distinguished from CSL boundaries. The BM specimen with the CSL boundary fraction of 56.4% shows a highly connected random boundary network. The grain size with and without considering twin boundaries in BM is 14 ± 3 μm and 24 ± 8 μm, respectively.

Figure 2 The maps (step size 1 μm) of **a** GBCD and **b** IPF for BM specimen shown by OIM images.

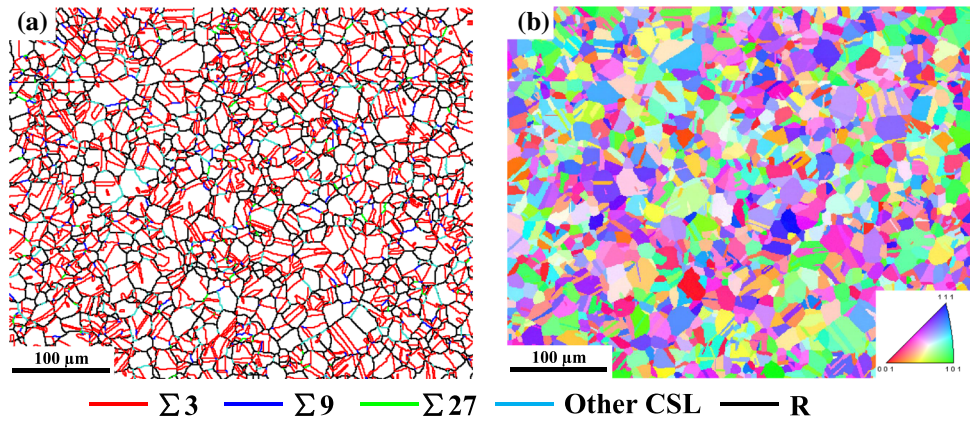
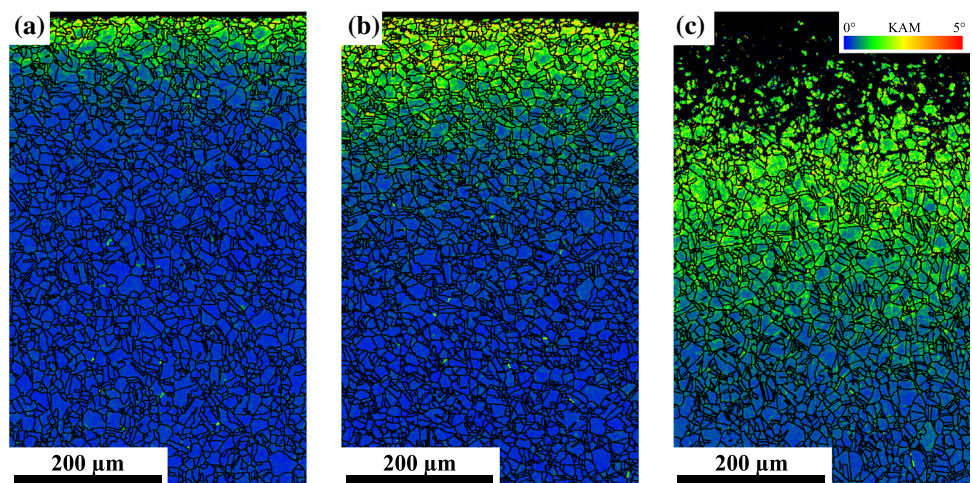


Figure 3 shows the Kernel Average Misorientation (KAM) colored maps on the cross section of SMGT specimens with various penetration depths. KAM is calculated by the local misorientation of a given point compared with all of its neighbors during the EBSD analysis. The KAM map can be used to examine the plastic strain distribution. It is obvious that the SMGT processing with a rotary tool refines the original grains near the surface and induces a typical gradient plastic deformation layer by one pass processing. The plastic strain and its depth increase with the increase in penetration depth. For the SMGT specimen with the penetration depth of 60 μm , the region near the surface is difficult to identify due to the severe plastic strain. Given the analytical relationship between hardness and plastic strain [38], the plastic strain distribution could be quantified by the hardness distribution along depth. Figure 4 shows the Vickers hardness distributions along the depth of cross sections perpendicular to the surface in SMGT specimens. The Vickers hardness of BM specimen is $195 \pm$

5 Hv, as indicated by blue dashed line in Fig. 4. The Vickers hardness profiles present a decreasing variation with depth from surface. The depths of plastic strain increase with the increase in penetration depths. The average depths of deformation layer induced by SMGT processing with the penetration depths of 20 μm , 40 μm and 60 μm reach to approximately 400 μm , 600 μm and 900 μm , respectively.

The optimized GBCD maps of cross sections in the near-surface layer for SMGT-GBEM specimens with various penetration depths after annealing at 900 $^{\circ}\text{C}$ for 96 h are presented in Fig. 5. It is obvious that there exist surface GBE regions with a high proportion of CSL boundaries and disconnected random boundary network for all the SMGT-GBEM specimens. The low energy boundaries, such as $\Sigma 3$, $\Sigma 9$, $\Sigma 27$ and other CSL boundaries as shown in Fig. 5(g), can be introduced into high energy random boundaries during twin events and reactions in thermomechanical process [25]. The introduced $\Sigma 3^n$ boundaries in random boundaries disrupt the connectivity of random

Figure 3 KAM colored maps (step size 1 μm) on the cross section of SMGT specimens with various penetration depths: **a** 20 μm , **b** 40 μm , **c** 60 μm .



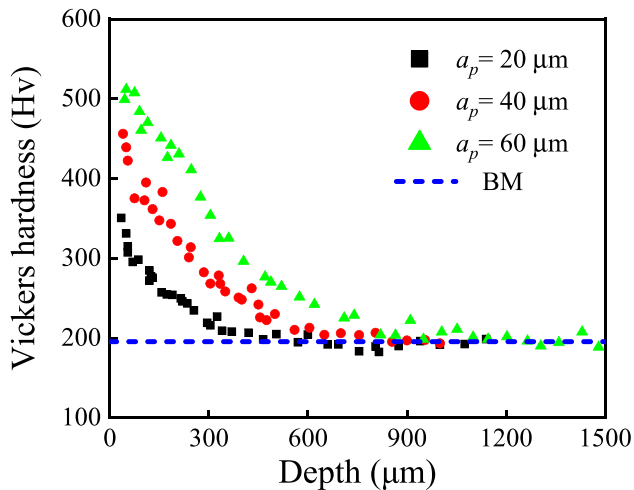


Figure 4 Hardness distributions along depth from surface in SMGT specimens with various penetration depths compared with BM specimen.

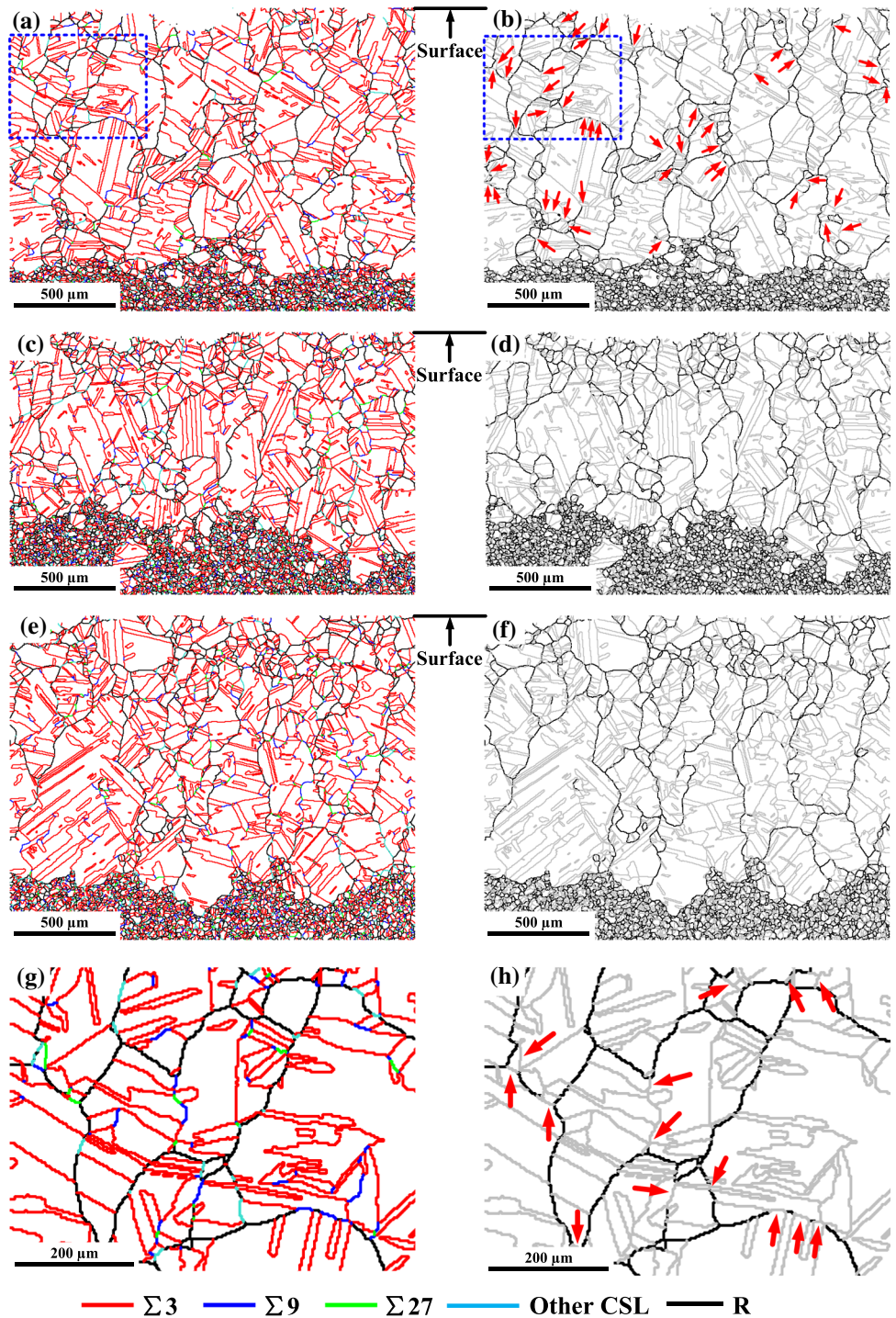
boundary network, as exemplarily indicated by the red arrows in Fig. 5(b) and (h). The frequency of boundaries for BM and SMGT-GBEM specimens are shown in Fig. 6 (a). For all SMGT-GBEM specimens, an optimized GBCD with over 75% frequency of CSL boundaries has been achieved after annealing. The fraction of CSL boundaries for SMGT-GBEM specimens with the penetration depths of 20 μm , 40 μm and 60 μm reaches to 78.2%, 76.3% and 78.1%, respectively. The increase in the fraction of CSL boundaries is mainly attributed to the formation of a high proportion ($\sim 70\%$) of $\Sigma 3$ twin boundaries, and statistical significance of twin-related boundaries ($\Sigma 9$ and $\Sigma 27$) was not observed. The fraction of special boundaries ($\Sigma 3^n$) for SMGT-GBEM specimens with $a_p = 20, 40$ and $60 \mu\text{m}$ reaches to 76.2%, 73.7% and 76.6%, respectively.

After 96 h annealing, heterogeneous grain growth, usually described as abnormal grain growth, and large size grain clusters with a high proportion of $\Sigma 3^n$ -type boundaries were observed in surface GBE regions, as easily identified in Fig. 5(b), (d) and (f). These clusters of grains have been described as "twin-related domains" or "grain clusters" [39–42]. The size and distribution of grain clusters are presented in Fig. 6. It is obvious that the size of grain clusters in SMGT-GBEM specimens is much larger than that of BM specimen and the grain clusters with large size ($\geq 200 \mu\text{m}$) are predominant in the surface GBE region. Fig. 7 shows the hardness distributions along depth for SMGT-GBEM specimens compared

with BM specimen. The region with larger grain clusters has a lower hardness, and the growth of grain clusters in surface GBE layer leads to decrease in the average hardness. Surface softening was introduced into surface layer because of larger grain size in SMGT-GBEM specimens compared to BM specimen. The spatially adjacent twin grains are the integral part of grain cluster, and these twinned-related grain clusters are the prominent feature of surface GBE microstructure. The crystallographic boundaries of neighboring grain clusters are frequently random boundaries. The SMGT-GBEM specimen with the penetration depth of 20 μm exhibits a relatively uniform dispersion of grain clusters in the grain size distribution. For the SMGT-GBEM specimens with the penetration depth of 40 μm and 60 μm , relatively small grain clusters and high density of random boundaries were observed in the near-surface region which is much deeper than the grain refinement region. However, there is a higher CSL% value of 81% within the depth of 200–800 μm and 84.5% within the depth of 400–1200 μm from surface for the SMGT-GBEM specimens with the penetration depth of 40 μm and 60 μm , respectively.

Previous GBE studies in 304 stainless steels have shown that low-level pre-strain ($< 10\%$) followed by long-time annealing resulted in the GBCD containing a high fraction of $\Sigma 3^n$ boundaries, while medium-level pre-strain (20%–50%) might be prone to introduce a higher fraction of random boundaries [13, 18]. The distribution of large size grain clusters and high fraction of $\Sigma 3^n$ boundaries in SMGT-GBEM specimens is compatible with the depth of low-level plastic strain induced by SMGT. In other words, the increased penetration depth resulted in the larger depth of low-level plastic strain, promoting the formation of higher fraction of $\Sigma 3^n$ boundaries and larger size grain clusters. Meanwhile, the severe plastic strain introduced relatively high fraction of random boundaries and small size grain clusters into near-surface region. In addition, the depths of surface GBE region for all the SMGT-GBEM specimens remain essentially consistent and are larger than the depth of plastic strain induced by SMGT. It suggests that the larger depth of gradient plastic strain has a minor effect on the thickness of surface GBE region after long-time annealing. The depth of gradient plastic strain ($\sim 300 \mu\text{m}$) for surface milling specimen [43] is close to that for SMGT specimen with the penetration depth of 20 μm . This provides the possibility of

Figure 5 Optimized GBCD maps (step size 3 μm) of SMGT specimens with various penetration depths after annealing at 900 $^{\circ}\text{C}$ for 96 h: **a–b** 20 μm , **c–d** 40 μm , **e–f** 60 μm . To highlight the random boundary network, $\Sigma 3^n$ boundaries are indicated by thin gray lines in **b**, **d** and **f**. **g–h** The enlarged images of the area marked in **a** and **b** by blue dash lines, respectively. The interruption of random boundary network by $\Sigma 3^n$ boundaries is exemplarily pointed out by red arrows in **b** and **h**.



applying the most common surface mechanical machining, such as milling and turning, as a pre-straining method in thermomechanical processing to implement surface GBE.

Intergranular corrosion resistance of optimized GBCD

The intergranular corrosion resistance of the BM and SMGT-GBEM specimens was evaluated by ferric sulfate-sulfuric acid corrosion test. During the corrosion test, the corrosion rate of SMGT-GBEM

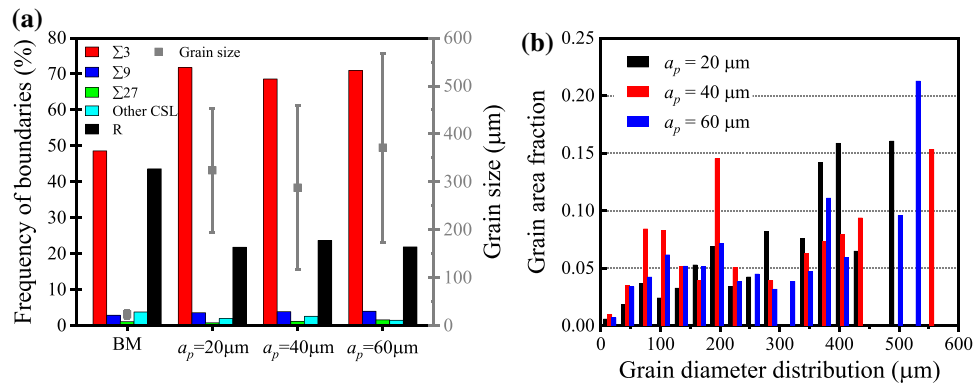


Figure 6 Statistics of microstructural characteristics for BM specimen and SMGT-GBEM specimens: **a** Frequency of boundaries and grain size without considering twin boundaries; **b** Grain size distribution without considering twin boundaries. Note that, frequency of boundaries and grain size are counted from

the depth of 0–1200 μm for SMGT specimens with $a_p = 20 \mu\text{m}$ and $a_p = 60 \mu\text{m}$ and the depth of 0–800 μm for SMGT specimen with $a_p = 40 \mu\text{m}$, respectively.

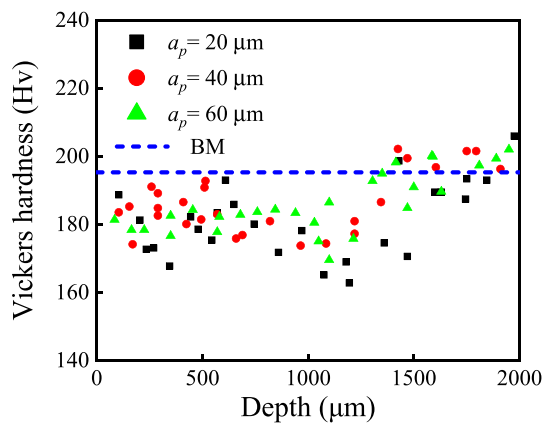


Figure 7 Hardness distributions along depth from surface in SMGT-GBEM specimens with various penetration depths compared with BM specimen.

specimens containing both surface GBE and non-GBE regions mainly depends on the mass loss of non-GBE regions. Thus, the corrosion rate is hard to quantitatively reflect the three-dimensional corrosion damage for surface GBE specimen with comparison to bulk GBE. For better comparison of intergranular corrosion resistance between surface GBE region and inner non-GBE region, the cross section perpendicular to the surface of SMGT-GBEM specimen was grounded to 2000 grit using series of waterproof papers and mechanically polished, then also tested for 72-h ferric sulfate-sulfuric acid corrosion. Figures 8 and 9 show the surface and cross section corrosion micrographs of BM and SMGT-GBEM specimens after 72-h ferric sulfate-sulfuric acid test. It is remarkable that the surface of BM specimen has

rather bad integrity with serious grain dropping due to the intergranular corrosion, as indicated in Fig. 8(a). In contrast, the surface of SMGT-GBEM specimen still retains the surface flatness with the typical corrosion along grain boundaries. The cross section corrosion micrographs indicate that the penetration depth of intergranular corrosion from surface is arrested in the surface GBE region within the corrosion depth of $250 \pm 20 \mu\text{m}$ as shown in Fig. 9(b), while the corrosion depth of BM specimen cannot be identified due to the serious grain dropping. Figure 9(c) shows the remarkable corrosion difference between the GBE region and non-GBE region after 72-h ferric sulfate-sulfuric acid test. There is a serious grain dropping in non-GBE region with the corrosion depth of approximately $550 \pm 50 \mu\text{m}$. However, only about $200 \pm 20 \mu\text{m}$ penetration depth along grain boundaries and no grain dropping were observed in GBE region. These results indicate that the SMGT-GBEM specimen with the optimized GBCD in surface region exhibits much better resistance to intergranular corrosion than the BM specimen.

To better understand the effect of optimized GBCD on the IGC behavior, the IGC morphologies in the cross section of SMGT-GBEM specimens with the penetration depth of 40 μm and 60 μm after oxalic acid electrolytic corrosion test are shown in Figs. 10 and 11. The types of grain boundaries in Figs. 10(c-e) and 11(c-d) were determined according to the GBCD maps of in Fig. 5(c) and (e), respectively. It is obvious that the network of corroded grain boundaries is essentially consistent with the random boundary

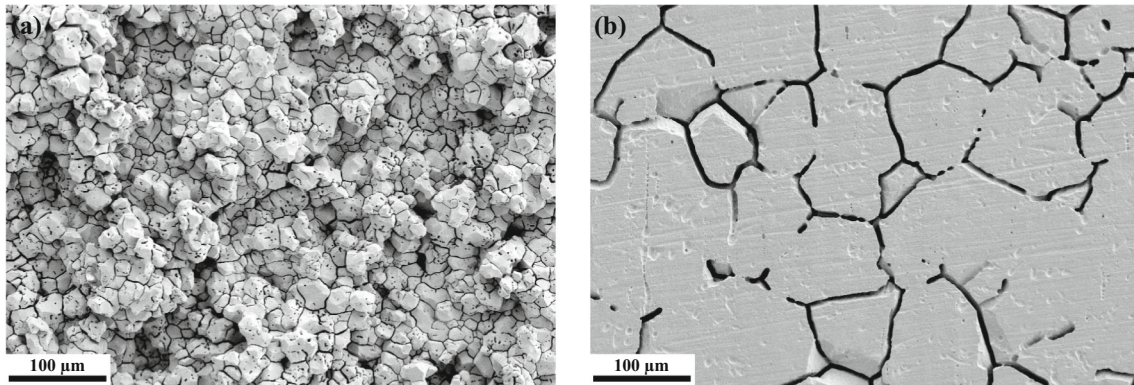


Figure 8 SEM images of surface corrosion micrographs after the 72-h ferric sulfate-sulfuric acid test: **a** BM and **b** SMGT-GBEM specimens.

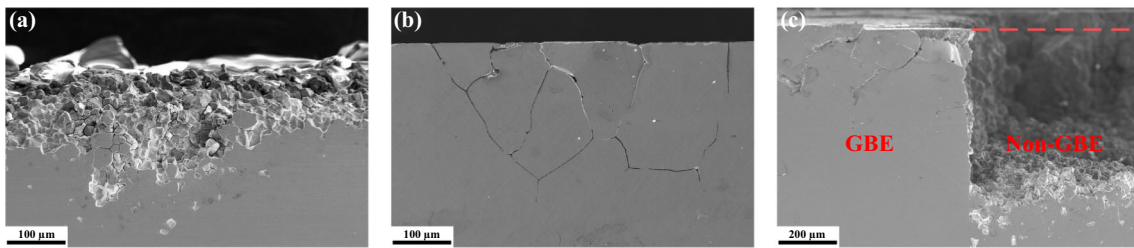


Figure 9 SEM images of cross section corrosion micrographs after the 72-h ferric sulfate-sulfuric acid test: **a** BM, **b** SMGT-GBEM and **c** cross section between surface region and inner non-

GBE region of SMGT-GBEM. The red dashed line in **c** represents the cross section perpendicular to the surface before the ferric sulfate-sulfuric acid test.

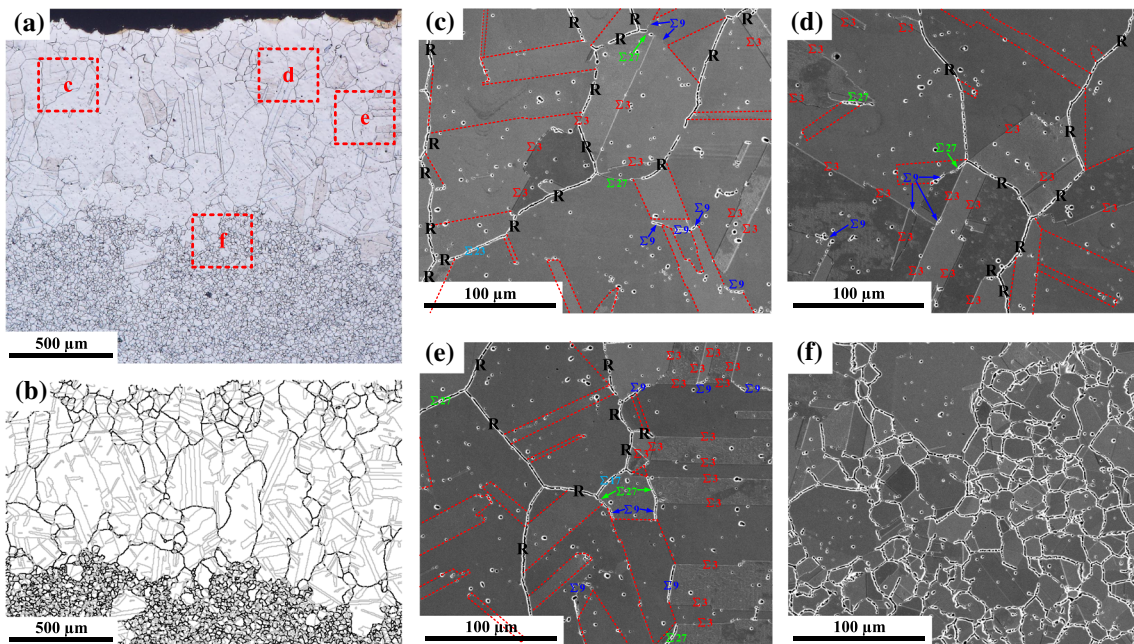


Figure 10 Intergranular corrosion morphologies of SMGT-GBEM specimen with the penetration depth of 40 μm after the oxalic acid electrolytic corrosion test: **a** Optical micrographs, **b** Corresponding GBCD at same location in **a**, **c** SEM image of the

area **c** marked in **a**, **d** SEM image of the area **d** marked in **a**, **e** SEM image of the area **e** marked in **a** and **f** SEM image of the area **f** marked in **a**. The red dash lines in **c–f** indicate the uncorroded $\Sigma 3$ twin boundaries.

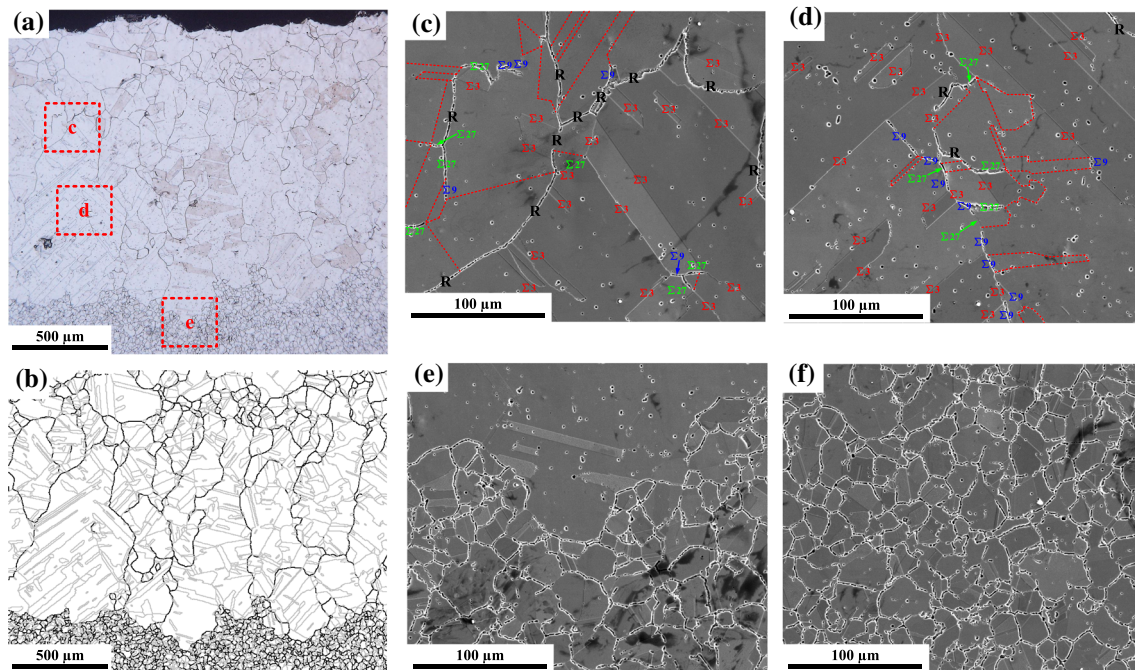


Figure 11 Intergranular corrosion morphologies of SMGT-GBEM specimen with the penetration depth of 60 μm after the oxalic acid electrolytic corrosion test: **a** Optical micrographs, **b** Corresponding GBCD at same location in **a**, **c** SEM image of the area **c** marked in

a, **d** SEM image of the area **d** marked in **a**, **e** SEM image of the area **e** marked in **a** and **f** SEM image of interior region below GBE region. The red dash lines in **c–d** indicate the uncorroded $\Sigma 3$ twin boundaries.

network. According to the optical micrographs, the density of corroded grain boundaries in inner non-GBE regions is much higher than that in surface GBE regions. Fig. 12 shows the statistics of corroded and uncorroded boundaries in the SMGT-GBEM specimens. Although the surface GBE regions have a great number twin boundaries (about 70% by length), twin boundaries in grain clusters are essentially free from corrosion, indicating an excellent corrosion resistance to IGC. In contrast, nearly all random boundaries exhibit serious corrosion, showing a significant susceptibility to IGC. Other special boundaries, such as $\Sigma 9$ and $\Sigma 27$, are also attacked which are similar to random boundaries. Despite the remarkable corrosion of non- $\Sigma 3$ twin boundaries, a few grain boundaries, such as $\Sigma 9$, $\Sigma 27$ in Fig. 10(c) and random boundaries in Fig. 11(c), exhibit essentially no corrosion. The corroded grain boundary network is mainly composed of the random boundaries and can be disrupted by these $\Sigma 3$ -type boundaries with improved corrosion resistance. The $\Sigma 3$ twin boundaries in $\Sigma 3$ -type grain boundaries exhibit an excellent and stable resistance to IGC in comparison with other CSL boundaries. Compared to random boundaries, $\Sigma 3$ twin boundaries with a smaller

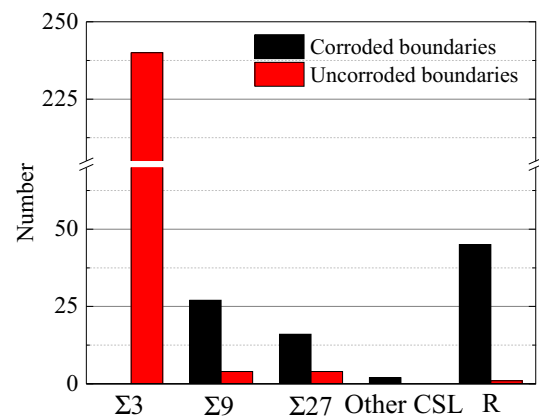


Figure 12 Statistics of corroded and uncorroded boundaries in surface GBE regions as indicated in Figs. 10 and 11.

chromium depletion zone result in the discontinuity of chromium depletion along the random boundary network and arrest the intergranular corrosion [44]. Gertsman et al. [45] and Hu et al. [6] also found that only coherent twin $\Sigma 3$ boundaries could be termed as special boundaries to resistance to IGC and IGSCC.

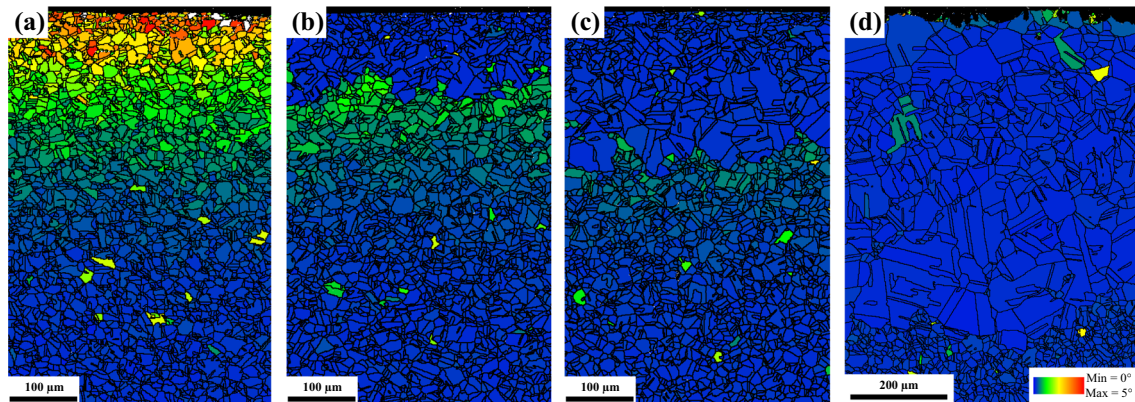


Figure 13 GOS colored maps (step size 1 μm) showing the plastic strain distributions of SMGT specimens with the penetration depth of 40 μm after various annealing time: **a** initial state, **b** 0.5 h, **c** 12 h and **d** 24 h.

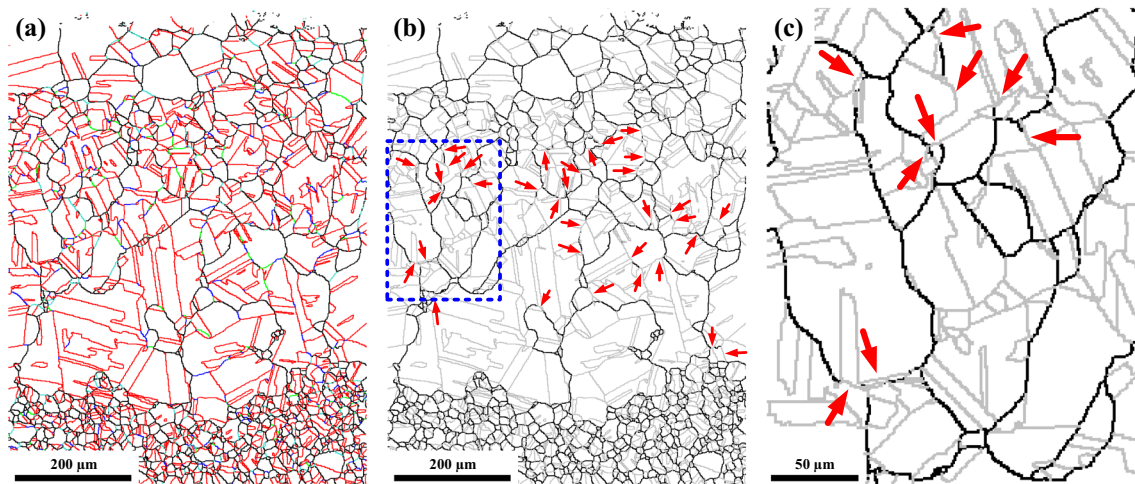


Figure 14 Optimized GBCD maps (step size 1 μm) of SMGT specimen with the penetration depth of 40 μm after annealing at 900 $^{\circ}\text{C}$ for 24 h. The $\Sigma 3^n$ boundaries are indicated by thin gray lines in **b** and the enlarged image of the area marked in **b** by blue

dash lines is shown in **c**. Red arrows point out the $\Sigma 3^n$ boundaries in random boundary network within the depth of 300–600 μm from surface.

Microstructure evolution during thermomechanical process

Recrystallization and grain growth are known to occur and can be strongly enhanced by pre-strain during the thermomechanical process [13]. In order to figure out the evolution of microstructure for SMGT specimens during the annealing process, EBSD observation and optical micrographs were conducted using the SMGT specimens with the penetration depth of 40 μm followed by annealing at 900 $^{\circ}\text{C}$ for various times. The grain orientation spread (GOS) is calculated by averaging the deviation between the orientation of each point in a given grain and the average orientation of that grain. Hence, GOS

can be used to examine the changes of plastic strain in grains of SMGT specimens after various annealing time. Figure 13 shows the GOS colored maps of SMGT specimens after annealing at 900 $^{\circ}\text{C}$ for 0–24 h. The GOS map of SMGT specimen indicates a typical gradient plastic strain distribution introduced by SMGT, as shown in Fig. 13(a). After annealing at 900 $^{\circ}\text{C}$ for 0.5 h, surface region within 100 μm has a fully recrystallized microstructure which is indicated by an average GOS level below 0.5 $^{\circ}$ [42, 46]. Meanwhile, the plastic strain in interior region below 100 μm from surface is not essentially consumed. The intermediate annealing steps of 0.5 h, 12 h and 24 h indicate that the grain clusters initiate from strain recrystallization in the near-surface layer and expand into low-level

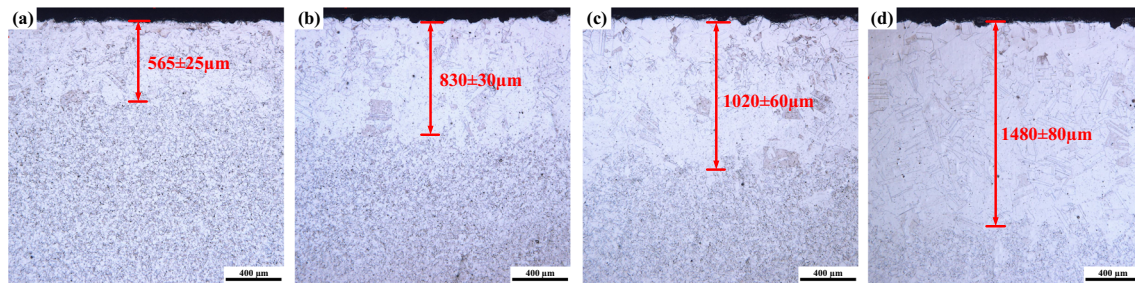


Figure 15 Optical micrographs of SMGT specimens with the penetration depth of 40 μm after various annealing time: **a** 24 h, **b** 48 h, **c** 72 h and **d** 96 h.

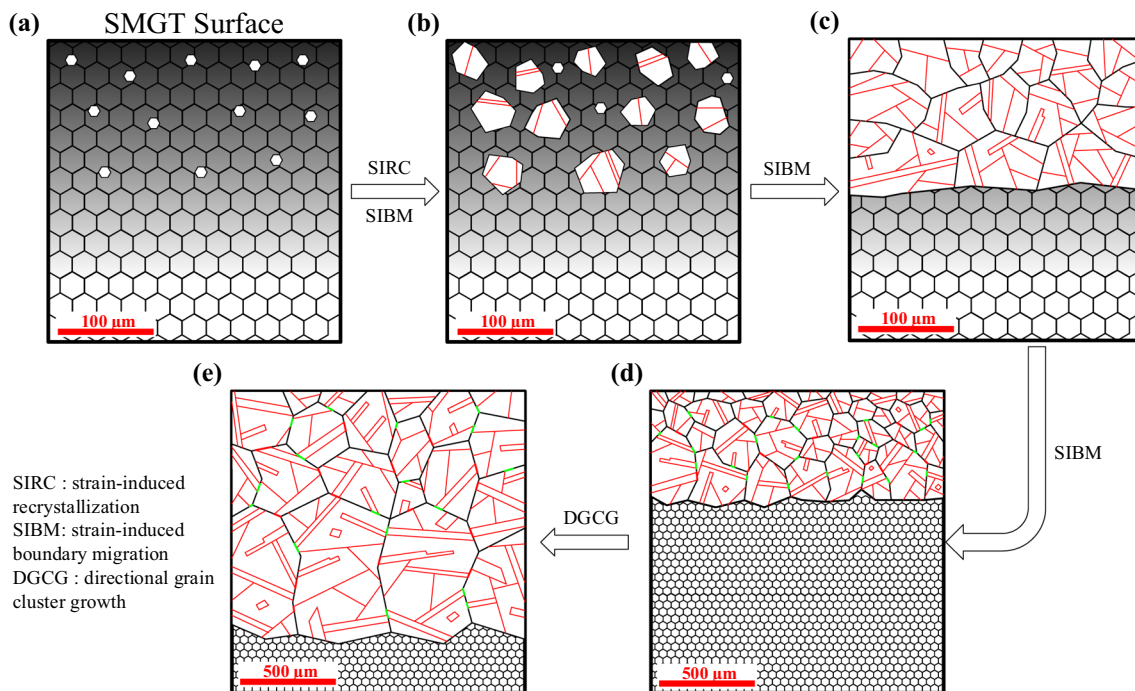


Figure 16 Schematic of the evolution of GBCDs in SMGT specimens during the annealing process. The sequence of images from (a) to (e) illustrate a time path of the strain-induced recrystallization, strain-induced boundary migration and directional grain cluster growth process. The gradient plastic

deformation regions by strain-induced boundary migration (SIBM) with the increase in annealing time, as illustrated in Fig. 13(b-d). The observed growth of grain clusters provides an opportunity for the formation of $\Sigma 3^n$ grain boundaries [42]. The distribution of GOS in Fig. 13(d) shows that the SMGT-induced plastic strain has been essentially depleted after annealing for 24 h.

The optimized GBCD maps of SMGT specimen after annealing at 900 $^{\circ}\text{C}$ for 24 h are presented in Fig. 14. The frequency of CSL boundaries and $\Sigma 3^n$ boundaries in the depth of 300–600 μm from surface

strain is colored in gray scale and the white is considered a strain-free grains. The black line represents the random grain boundaries and the red line represents the $\Sigma 3^n$ ($n \geq 1$) grain boundaries. The green lines in (d) and (e) indicate the other CSL boundaries in random boundary network.

reaches 75.7% and 73.4%, respectively. The connectivity of random boundary network is interrupted by $\Sigma 3^n$ boundaries as indicated by the red arrows in Fig. 14 (b) and (c). The SIBM can effectively optimize the GBCD by the formation of numerous annealing twins behind the migration front and the introduction of low energy segments in random boundary network during the annealing process [25, 26]. Xia et al. [40] also found that the strain deformation in Alloy 690 could induce recrystallization and the large twin-related grain clusters formed from a single nucleus. The strain recrystallization and subsequent

SIBM process dominate the optimization of GBCD in the near-surface layer for SMGT-GBEM specimen during the early annealing process within 24 h.

Figure 15 shows the optical micrographs of SMGT specimens after annealing at 900 °C for 24–96 h. It is obvious that the thickness of surface GBE region increases with annealing time at a growth rate of 200–400 μm per 24 h. It indicates that the thickness of surface GBE region can be regulated by the annealing time. As the surface GBE region grows, numerous annealing twins form and the size of grain clusters increases while the grain size of non-GBE region in specimen interior remains unchanged, as also indicated in Fig. 5. During the long-time annealing process, the formed grain clusters in the near-surface layer, as shown in Fig. 14, directionally grow into the specimen interior. It is notable that the plastic strain has been essentially depleted after annealing at 900 °C for 24 h. Koo et al. [47] have reported that the low-level deformation activates the rapid migration of grain boundaries, promoting the abnormal grain growth to occur in coarse grained pure Cu. Booth et al. [48] indicated that the nucleation and growth of twinning are mechanistically linked to anomalous grain growth, and the length fraction of annealing twins increases with annealing time. The abnormal grain growth at a relatively low temperature probably plays an essential role in the directional growth of grain clusters during the long-time annealing process [25]. The low energy of twin boundaries makes them easily form and keep in the abnormal grain growth, while the random boundaries migrate widely and interact with other boundaries. The microstructure difference in grain boundary type and density between surface GBE region and material interior probably results in the directional growth of grain clusters [49–51].

Figure 16 outlines the proposed qualitative mechanism for the evolution of GBCDs in SMGT specimens during the annealing process. The microstructure evolution for SMGT specimens during annealing at 900 °C could be presumed in the following way. The gradient plastic strain is initially introduced by SMGT, and the severe plastic strain near the surface activates the strain recrystallization at the beginning of annealing, as shown in Fig. 16(a). The gradient plastic strain over the critical strain value for recrystallization determines a gradient distribution of the number density of nucleation sites. The grain boundary migration induced by plastic

strain is consecutively activated near nucleation sites, resulting in the growth of new grains, as illustrated in Fig. 16(b). The formed grains with free of strain grow with the consumption of strain energy until collision with other newly recrystallized grains or strain-free area. Annealing twins inside growing grains are highly prone to form due to their low energy. The higher-order twin-related boundaries have been experimentally observed to form when two separate parts of a growing twin-related grain cluster impinge upon one another [13]. Other CSL boundaries may be formed at random boundary network with the accompany of grain boundary migration [25]. As the complete depletion of SMGT-induced plastic strain, twin-related grain clusters with a high proportion of CSL boundaries and disconnected random boundary network are formed, as illustrated in Fig. 16(d). Subsequently, the directional growth of grain clusters during the long-time annealing process promotes further extension of surface GBE region into material interior. The dynamic evolution of the surface microstructure during the annealing process in this study is hard to be observed in situ based on our current experiment techniques. Thus, further experimental study is needed to classify the mechanisms involved in the annealing process, in particular the directional growth of grain clusters.

Conclusions

In this work, an effective and economical method was applied to optimize grain boundary character distribution in the near-surface layer for 304 stainless steel. The SMGT with a rotary tool as a surface gradient plastic pre-straining method and subsequently annealing at 900 °C for 24–96 h achieved a surface GBE region with a high proportion of CSL boundaries in excess of 75% and disconnected random boundary network. The SMGT-GBEM specimens demonstrated an excellent resistance to intergranular corrosion during the ferric sulfate-sulfuric acid tests. The oxalic acid electrolytic corrosion tests showed that the improvement of resistance to IGC results from the optimized GBCD with a high proportion of $\Sigma 3^{\text{n}}$ boundaries and discontinuity of the random boundary network. During the annealing process, severe plastic strain near the surface results in relatively high fraction of random boundaries and small size grain clusters via strain recrystallization, while

low-level plastic strain in the subsurface promotes the formation of high fraction of CSL boundaries and large size grain clusters via strain-induced boundary migration. After the complete depletion of SMGT-induced plastic strain, the directional growth of grain clusters during the long-time annealing process promotes further extension of surface GBE region into material interior, and the thickness of surface GBE region can be regulated by the annealing time. The gradient plastic strain induced by mechanical machining and followed annealing pave a new pathway to optimize the GBCD in the near-surface layer, which has great potential for engineering application of GBE in complicated machining surface.

Acknowledgements

This work was supported by the National Natural Science Foundation of China [grant number 51875219] and the Scientific Research Project of Hubei Provincial Department of Education (grant number Q20239404).

Author Contributions

Xinli Jiang contributed to conceptualization, methodology, software, writing—original draft. Chongwen Yang contributed to methodology, visualization. Wenqian Zhang contributed to software, reviewing, editing. Xuelin Wang contributed to reviewing, editing, supervision, funding acquisition.

Data availability

The data supporting the findings of this study are available upon reasonable request.

Declarations

Conflict of interest The authors declare that there are no conflicts of interest.

References

- [1] Watanabe T (1978) An approach to grain boundary design for strong and ductile polycrystals. *Res MechInt J Struct Mech Mater Sci* 11(1):47–84
- [2] Palumbo G, Lehockey EM, Lin P (1998) Applications for grain boundary engineered materials. *JOM* 50(2):40–43. <https://doi.org/10.1007/s11837-998-0248-z>
- [3] Watanabe T (2011) Grain boundary engineering: historical perspective and future prospects. *J Mater Sci* 46(12):4095–4115. <https://doi.org/10.1007/s10853-011-5393-z>
- [4] Bozzolo N, Bernacki M (2020) Viewpoint on the Formation and evolution of annealing twins during thermomechanical processing of FCC metals and alloys. *Metall Mater Trans A* 51(6):2665–2684. <https://doi.org/10.1007/s11661-020-05772-7>
- [5] Michiuchi M, Kokawa H, Wang Z, Sato Y, Sakai K (2006) Twin-induced grain boundary engineering for 316 austenitic stainless steel. *Acta Mater* 54(19):5179–5184. <https://doi.org/10.1016/j.actamat.2006.06.030>
- [6] Hu C, Xia S, Li H, Liu T, Zhou B, Chen W, Wang N (2011) Improving the intergranular corrosion resistance of 304 stainless steel by grain boundary network control. *Corros Sci* 53(5):1880–1886. <https://doi.org/10.1016/j.corsci.2011.02.005>
- [7] West E, Was G (2009) IGSCC of grain boundary engineered 316L and 690 in supercritical water. *J Nucl Mater* 392(2):264–271. <https://doi.org/10.1016/j.jnucmat.2009.03.008>
- [8] Liu T, Xia S, Shoji T (2021) Intergranular stress corrosion cracking in simulated BWR water of 316L stainless steels manufactured with different procedures. *Corros Sci* 183:109344. <https://doi.org/10.1016/j.corsci.2021.109344>
- [9] Bechtle S, Kumar M, Somerday BP, Launey ME, Ritchie RO (2009) Grain-boundary engineering markedly reduces susceptibility to intergranular hydrogen embrittlement in metallic materials. *Acta Mater* 57(14):4148–4157. <https://doi.org/10.1016/j.actamat.2009.05.012>
- [10] Kobayashi S, Nakamura M, Tsurekawa S, Watanabe T (2011) Effect of grain boundary microstructure on fatigue crack propagation in austenitic stainless steel. *J Mater Sci* 46(12):4254–4260. <https://doi.org/10.1007/s10853-010-5238-1>
- [11] Kobayashi S, Yang W, Tomobe Y, Okada R, Tsurekawa S (2020) Low-angle boundary engineering for improving high-cycle fatigue property of 430 ferritic stainless steel. *J Mater Sci* 55(22):9273–9285. <https://doi.org/10.1007/s10853-020-04555-0>
- [12] Shi F, Tian P, Jia N, Ye Z, Qi Y, Liu C, Li X (2016) Improving intergranular corrosion resistance in a nickel-free and manganese-bearing high-nitrogen austenitic stainless steel through grain boundary character distribution optimization. *Corros Sci* 107:49–59. <https://doi.org/10.1016/j.corsci.2016.02.019>

- [13] Barr CM, Leff AC, Demott RW, Doherty RD, Taheri ML (2018) Unraveling the origin of twin related domains and grain boundary evolution during grain boundary engineering. *Acta Mater* 144:281–291. <https://doi.org/10.1016/j.actamat.2017.10.007>
- [14] Guan X, Shi F, Ji H, Li X (2020) A possibility to synchronously improve the high-temperature strength and ductility in face-centered cubic metals through grain boundary engineering. *Scr Mater* 187:216–220. <https://doi.org/10.1016/j.scriptamat.2020.06.026>
- [15] Watanabe T, Tsurekawa S (2004) Toughening of brittle materials by grain boundary engineering. *Mater Sci Eng A* 387–389:447–455. <https://doi.org/10.1016/j.msea.2004.01.140>
- [16] Barr CM, Thomas S, Hart JL, Harlow W, Anber E, Taheri ML (2018) Tracking the evolution of intergranular corrosion through twin-related domains in grain boundary networks. *npj Mater Degrad* 2(1):14. <https://doi.org/10.1038/s41529-018-0032-7>
- [17] Kokawa H, Shimada M, Michiuchi M, Wang Z, Sato Y (2007) Arrest of weld-decay in 304 austenitic stainless steel by twin-induced grain boundary engineering. *Acta Mater* 55(16):5401–5407. <https://doi.org/10.1016/j.actamat.2007.06.005>
- [18] Fang X, Zhang K, Guo H, Wang W, Zhou B (2008) Twin-induced grain boundary engineering in 304 stainless steel. *Mater Sci Eng A* 487(1–2):7–13. <https://doi.org/10.1016/j.msea.2007.09.075>
- [19] Randle V, Coleman M (2009) A study of low-strain and medium-strain grain boundary engineering. *Acta Mater* 57(11):3410–3421. <https://doi.org/10.1016/j.actamat.2009.04.002>
- [20] Feng W, Yang S, Yan Y (2018) Effects of deformation mode and strain level on grain boundary character distribution of 304 Austenitic stainless steel. *Metall Mater Trans A* 49(6):2257–2268. <https://doi.org/10.1007/s11661-018-4589-0>
- [21] Randle V (1999) Mechanism of twinning-induced grain boundary engineering in low stacking-fault energy materials. *Acta Mater* 47(15–16):4187–4196. [https://doi.org/10.1016/s1359-6454\(99\)00277-3](https://doi.org/10.1016/s1359-6454(99)00277-3)
- [22] Lehockey EM, Palumbo G, Lin P (1998) Improving the weldability and service performance of nickel-and iron-based superalloys by grain boundary engineering. *Metall Mater Trans A* 29(12):3069–3079. <https://doi.org/10.1007/s11661-998-0214-y>
- [23] Thaveepungsriporn V, Sinsrok P, Thong-Aram D (2001) Effect of iterative strain annealing on grain boundary network of 304 stainless steel. *Scr Mater* 44(1):67–71. [https://doi.org/10.1016/s1359-6462\(00\)00582-0](https://doi.org/10.1016/s1359-6462(00)00582-0)
- [24] Kumar M, King WE, Schwartz AJ (2000), Modifications to the microstructural topology in f.c.c. materials through thermomechanical processing. *Acta Mater* 48 (9) 281–291. [https://doi.org/10.1016/s1359-6454\(00\)00045-8](https://doi.org/10.1016/s1359-6454(00)00045-8)
- [25] Shimada M, Kokawa H, Wang Z, Sato Y, Karibe I (2002) Optimization of grain boundary character distribution for intergranular corrosion resistant 304 stainless steel by twin-induced grain boundary engineering. *Acta Mater* 50(9):2331–2341. [https://doi.org/10.1016/S1359-6454\(02\)0064-2](https://doi.org/10.1016/S1359-6454(02)0064-2)
- [26] Yang X, Wang P, Huang M (2022) Grain boundary evolution during low-strain grain boundary engineering achieved by strain-induced boundary migration in pure copper. *Mater Sci Eng A* 833:142532. <https://doi.org/10.1016/j.msea.2021.142532>
- [27] Yang S, Wang ZJ, Kokawa H, Sato YS (2007) Grain boundary engineering of 304 austenitic stainless steel by laser surface melting and annealing. *J Mater Sci* 42(3):847–853. <https://doi.org/10.1007/s10853-006-0063-2>
- [28] Alyousif OM, Engelberg DL, Marrow TJ (2008) Surface grain boundary engineering of shot-peened type 304 stainless steel. *J Mater Sci* 43(4):1270–1277. <https://doi.org/10.1007/s10853-007-2252-z>
- [29] Tokita S, Kokawa H, Kodama S, Sato YS, Sano Y, Li Z, Feng K, Wu Y (2020) Suppression of intergranular corrosion by surface grain boundary engineering of 304 austenitic stainless steel using laser peening plus annealing. *Mater Today Commun* 25:101572. <https://doi.org/10.1016/j.mtcomm.2020.101572>
- [30] Telang A, Gill AS, Tammana D, Wen X, Kumar M, Teysseyre S, Mannava SR, Qian D, Vasudevan VK (2015) Surface grain boundary engineering of Alloy 600 for improved resistance to stress corrosion cracking. *Mater Sci Eng A* 648:280–288. <https://doi.org/10.1016/j.msea.2015.09.074>
- [31] Davim JP et al (2010) Surface integrity in machining. Springer, USA
- [32] Li W, Tao N, Lu K (2008) Fabrication of a gradient nano-micro-structured surface layer on bulk copper by means of a surface mechanical grinding treatment. *Scr Mater* 59(5):546–549. <https://doi.org/10.1016/j.scriptamat.2008.05.003>
- [33] Zeng Z, Li X, Xu D, Lu L, Gao H, Zhu T (2016) Gradient plasticity in gradient nano-grained metals. *Extrem Mech Lett* 8:213–219. <https://doi.org/10.1016/j.eml.2015.12.005>
- [34] Kokawa H, Shimada M, Sato YS (2000) Grain-boundary structure and precipitation in sensitized austenitic stainless steel. *JOM*. <https://doi.org/10.1007/s11837-000-0159-0>
- [35] Brandon D (1966) The structure of high-angle grain boundaries. *Acta Metall* 14(11):1479–1484. [https://doi.org/10.1016/0001-6160\(66\)90168-4](https://doi.org/10.1016/0001-6160(66)90168-4)

- [36] Kokawa H, Watanabe T, Karashima S (1987) Reexamination of deviation angles from exact CSL misorientations in early work on grain boundary characterization. *Scr Metall* 21(6):839–842. [https://doi.org/10.1016/0036-9748\(87\)90333-4](https://doi.org/10.1016/0036-9748(87)90333-4)
- [37] Lee JJB (1983) Modification of the ASTM standard ferric sulfate-sulfuric acid test and copper-copper sulfate-sulfuric acid test for determining the degree of sensitization of ferritic stainless steels. *Corrosion* 39(12):469–474. <https://doi.org/10.5006/1.3577368>
- [38] Sonmez FO, Demir A (2007) Analytical relations between hardness and strain for cold formed parts. *J Mater Process Technol* 186(1–3):163–173. <https://doi.org/10.1016/j.jmatprotec.2006.12.031>
- [39] Reed BW, Kumar M (2006) Mathematical methods for analyzing highly-twinned grain boundary networks. *Scr Mater* 54(6):1029–1033. <https://doi.org/10.1016/j.scriptamat.2005.11.045>
- [40] Xia S, Zhou B, Chen W (2008) Effect of single-step strain and annealing on grain boundary character distribution and intergranular corrosion in Alloy 690. *J Mater Sci* 43(9):2990–3000. <https://doi.org/10.1007/s10853-007-2164-y>
- [41] Bober DB, Lind J, Mulay RP, Rupert TJ, Kumar M (2017) The formation and characterization of large twin related domains. *Acta Mater* 129:500–509. <https://doi.org/10.1016/j.actamat.2017.02.051>
- [42] Tokita S, Kokawa H, Sato YS, Fujii HT (2017) In situ EBSD observation of grain boundary character distribution evolution during thermomechanical process used for grain boundary engineering of 304 austenitic stainless steel. *Mater Charact* 131:31–38. <https://doi.org/10.1016/j.matchar.2017.06.032>
- [43] Zhang W, Wang X, Hu Y, Wang S (2018) Quantitative studies of machining-induced microstructure alteration and plastic deformation in AISI 316 stainless steel using EBSD. *J Mater Eng Perform* 27(2):434–446. <https://doi.org/10.1007/s11665-018-3129-9>
- [44] Yun Bi H, Kokawa H, Jie Wang Z, Shimada M, Sato YS (2003) Suppression of chromium depletion by grain boundary structural change during twin-induced grain boundary engineering of 304 stainless steel. *Scr Mater* 49(3):219–223. [https://doi.org/10.1016/S1359-6462\(03\)00261-6](https://doi.org/10.1016/S1359-6462(03)00261-6)
- [45] Gertsman V, Bruemmer S (2001) Study of grain boundary character along intergranular stress corrosion crack paths in austenitic alloys. *Acta Mater* 49(9):1589–1598. [https://doi.org/10.1016/S1359-6454\(01\)00064-7](https://doi.org/10.1016/S1359-6454(01)00064-7)
- [46] Schwartz AJ, Kumar M, Adams BL, Field DP (2009), *Electron backscatter diffraction in materials science*. Springer, USA <https://doi.org/10.1007/978-0-387-88136-2>
- [47] Koo JB, Yoon DY (2001) Abnormal grain growth in bulk Cu-The dependence on initial grain size and annealing temperature. *Metall Mater Trans A* 32(8):1911–1926. <https://doi.org/10.1007/s11661-001-0004-2>
- [48] Booth M, Randle V, Owen G (2005) Time evolution of sigma 3 annealing twins in secondary recrystallized nickel. *J Microsc* 217(2):162–166. <https://doi.org/10.1111/j.1365-2818.2005.01422.x>
- [49] Ueno K, Ritzdorf T, Grace S (1999) Seed layer dependence of room-temperature recrystallization in electroplated copper films. *J Appl Phys* 10(1063/1):371462
- [50] Harper JME, Cabral C, Andricacos PC, Gignac L, Noyan IC, Rodbell KP, Hu CK (1999) Mechanisms for microstructure evolution in electroplated copper thin films near room temperature. *J Appl Phys* 86(5):2516–2525. <https://doi.org/10.1063/1.371086>
- [51] Lee S, Yoon D, Henry M (2000) Abnormal grain growth and grain boundary faceting in a model Ni-base superalloy. *Acta Mater* 48(12):3071–3080. [https://doi.org/10.1016/S1359-6454\(00\)00119-1](https://doi.org/10.1016/S1359-6454(00)00119-1)

Publisher's Note Springer Nature remains neutral with regard to jurisdictional claims in published maps and institutional affiliations.

Springer Nature or its licensor (e.g. a society or other partner) holds exclusive rights to this article under a publishing agreement with the author(s) or other rightsholder(s); author self-archiving of the accepted manuscript version of this article is solely governed by the terms of such publishing agreement and applicable law.